Observation of topological Floquet states interference

Chengrui Ji,[1] Shaodong Zhou,[1] An Xie,[1] Zhenyu Jiang,[1] Xiaohang Sheng,[1] Li Ding,[1] Yongguan Ke,[2,3,*] Huaiqiang Wang,[4,5,†] Songlin Zhuang,[1] and Qingqing Cheng[1,‡]

[1]*School of Optical-Electrical and Computer Engineering, University of Shanghai for Science and Technology, Shanghai 200093, People's Republic of China*

[2]*Guangdong Provincial Key Laboratory of Quantum Metrology and Sensing & School of Physics and Astronomy, Sun Yat-Sen University (Zhuhai Campus), Zhuhai 519082, People's Republic of China*

[3]*International Quantum Academy, Shenzhen 518048, China*

[4]*School of Physics and Technology, Nanjing Normal University, Nanjing 210023, People's Republic of China*

[5]*National Laboratory of Solid State Microstructures, School of Physics, Nanjing University, Nanjing 210093, People's Republic of China*

(Received 9 May 2023; accepted 16 August 2023; published 24 August 2023)

Periodic modulation of the Hamiltonian offers a powerful method to engineer Floquet band properties and create new gaps capable of hosting Floquet edge modes. However, there have been limited studies exploring the performance of Floquet edge modes in terms of dynamic control and interference properties. Here, we experimentally implement an array of staggered coupled plasmonic waveguides operating at microwave frequencies based on the Floquet Su-Schrieffer-Heeger model. Our observations reveal the coexistence of Floquet zero and π modes within a specific periodic range of the quasienergy spectrum. Through near-field experiments, we observe a subharmonic response of the electric field propagation in the microwave, which is confirmed by the interference of eigenfields associated with the two topological end modes. Our work not only provides an approach for studying time-dependent Floquet Hamiltonians, but also opens the door to exploring period-doubling nonequilibrium topological phases.

DOI: 10.1103/PhysRevB.108.054310

I. INTRODUCTION

Topological states in periodically driven systems have rapidly emerged as a thriving research area in recent years [1–6]. In contrast to static systems, energy conservation is absent in periodically driven systems. Instead, the concept of quasienergy [7,8] is introduced, which is defined modulo $2\pi/\Lambda$, where Λ represents the period of the driving potential. The topological properties of periodically driven systems are extracted from the quasienergy bands, which capture the system's dynamics at multiples of driving period. Novel topological phases are identified by topological invariants of the quasienergy bands such as Chern numbers [9,10], and by the emergence of edge states [11,12]. Using the Floquet band theory, Floquet topological insulators [13,14], as dynamical analogues of topological insulators, have been theoretically predicted and experimentally demonstrated in a variety of platforms, including electronic [15–17], cold atomic [18–20], and photonic systems [21–23]. In particular, periodic modulation has enhanced the field of topological photonics and motivated potential applications of topological photonic devices [24].

Manipulating the driving frequency or amplitude can induce topological phase transitions, leading to robust and highly controllable light transport. In photonic systems, periodic driving has been used to investigate static network systems, which can be mapped onto a Floquet lattice [25,26]. In the adiabatic regime, topological pumps through bulk and edge channels have been observed [27–30]. In suitable driving regimes, there are rich anomalous topological phases, gauge dependence, and Floquet phase transitions [31]. In the higher frequency regime, effective Hamiltonian governing stroboscopic dynamics has been used to predict novel topological properties, which are typically inaccessible in static systems [32,33].

Most existing references focus on Floquet topological edge states [4,14,34–38]. Taking the proof-of-principle Floquet Su-Schrieffer-Heeger (SSH) model as an example, there are two distinct types of topological boundary modes: the topological zero modes and the topological π modes, residing within the zero and π quasienergy gaps, respectively. These two types of topological boundary states originate from different global effects. The topological π mode arises due to the alternating change between the two kinds of modes in the SSH model, namely the bulk modes and boundary modes [39,40]. On the other hand, the topological zero mode can be regarded as arising from an existing nontrivial topological phase without modulation [41,42]. However, the study of the coexistence and interplay between the different modes remains largely unexplored [38]. It is important to understand the dynamic control and coexistence of the two kinds of Floquet modes and the interference between them. Addressing these challenges requires a versatile experimental platform capable of facile frequency tuning and realizing the

*keyg@mail2.sysu.edu.cn
†hqwang@nju.edu.cn
‡qqcheng@usst.edu.cn

coexistence of Floquet zero and π modes. Photonic systems, particularly waveguide arrays, have emerged as powerful tools for investigating Floquet topological systems [39,43,44].

In our work, we conducted a joint experimental and theoretical investigation of the driven SSH model with time-periodic staggered coupling constants. Our experimental implementation of the model utilized evanescently coupled spoof surface plasmonic polariton (SPP) waveguides operating at microwave frequencies [45–51]. SPPs are special electromagnetic waves in the optical frequency region, which are bound on the metal/dielectric interface. To realize high-confinement SPPs at low frequency, plasmonic metamaterials have been proposed, in which the corrugated metallic structures are efficient models to support and propagate spoof SPPs in microwave bands [46]. By exploiting the coexistence of Floquet topological π modes and zero edge mode localization at the system boundary, we were able to unambiguously identify the interference property. The beating phenomenon in our system gives rise to subharmonic dynamics, characterized by a stable period-2Λ oscillation. The stroboscopic dynamics can be derived by superimposing the eigenfields within a certain range of driving frequencies in the quasienergy spectrum. Our work provides a periodic modulation approach that allows switching between the three topological states of Floquet zero, π, and the coexistence of these states.

II. FLOQUET SSH MODEL

We employ the driven SSH model to demonstrate the existence of two distinct Floquet topological boundary modes. The Hamiltonian is given by

$$H = \sum_{m=1}^{N} c_m^{\dagger} c_m \times \beta_0 + \sum_{m=1}^{N-1} c_m^{\dagger} c_{m+1} \times [\kappa_0 + (-1)^m (\delta\kappa_0 + \delta\kappa(z))] + \text{H.c.} \quad (1)$$

Here, N represents the total number of waveguides, and β_0 denotes the propagation constant. The operators $c_m^{\dagger}$ and c_m correspond to the creation and annihilation operators of the mth waveguide, respectively. The second off-diagonal term in the equation represents the coupling strength κ between nearest-neighbor waveguides. The coupling strength consists of a constant term κ_0, a staggered term $\delta\kappa_0$, and the periodic variation of the coupling strength $\delta\kappa(z)$, which is given by

$$\delta\kappa(z) = \delta\kappa_1 \cos(2\pi z/\Lambda + \theta_0). \quad (2)$$

Here, $\delta\kappa_1$ represents the amplitude of the variation, Λ is the period of modulation, and θ_0 is the phase offset. Therefore, in our system, we observe that the Floquet regime is primarily governed by the parameter Λ. When the length of one period is much larger than the coupling length between the adjacent waveguides ($l_c = \pi/2\kappa_0$), the system can be considered to be corresponding to the adiabatic regime. However, as the length decreases and approaches the coupling length l_c, the system corresponds to the Floquet regime.

We implemented waveguide arrays that fulfill the requirements of the driven SSH model, with simplified diagrams illustrating the models depicted in Figs. 1(a) and 1(b). These arrays consist of ultrathin copper structures featuring coupled corrugated waveguides, which are bent and arranged as

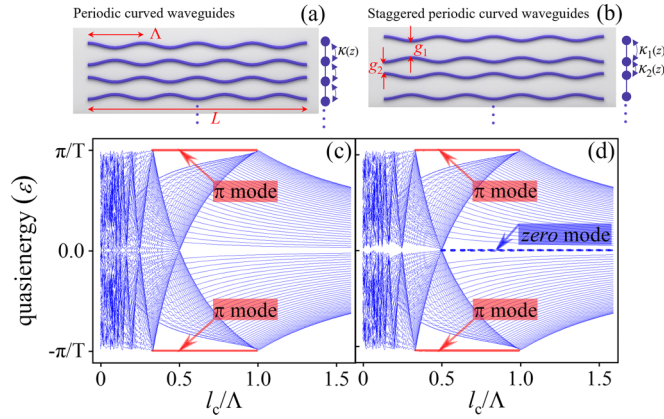

FIG. 1. Simplified diagram of a curved waveguide array and the quasienergy spectrum of the effective Hamiltonian. (a) and (c) show the situation where $g_1 = g_2$ and $\delta\kappa_0 = 0$,which corresponds to the maximum values of $\kappa_1(z)$ being the same as those of $\kappa_2(z)$. (b) and (d) show the situation where $g_1 > g_2$, which introduces a staggered term, $\delta\kappa_0 > 0$, leading to that the maximum value of $\kappa_1(z)$ is less that of $\kappa_2(z)$.

dictated by the model constraints. The spacings between adjacent waveguides follow a cosine function along the z axis. The array of ultrathin copper strips is printed on a dielectric film, thus providing an effective platform for propagating spoof SPP at microwave frequencies. Specifically, the position of one of the bending waveguides was determined by the function $x_0(z) = \pm A_0 \cos[(2\pi z/\Lambda) + \theta_0]$, where A_0, Λ, and θ_0 represent the amplitude, periodic length, and initial phase of the cosine curve, respectively. The spacing between the bending waveguides was designed to satisfy the condition $G(z) = g_a \pm g_o \pm 2A_0 \cos(2\pi z/\Lambda + \theta_0)$, where g_a and g_o denote the average and overall dimerization distances among the waveguide arrays. For the sake of simplicity, we define the minimum spacing between the first and second waveguides as g_1 and the minimum spacing between the second and third waveguides as g_2. Consequently, we can establish the relationship as $g_1 = g_a + g_o - 2A_0$ and $g_2 = g_a - g_o - 2A_0$. Furthermore, the effective coupling constant κ is connected to the gap distance (see the Supplemental Material [52] for details). When the magnitude of the staggered term $g_o \pm 2A_0 \cos(2\pi z/\Lambda + \theta_0)$ is much smaller than the average distance g_a, we can approximate the effective coupling constant as $\kappa = \kappa_0 \pm \delta\kappa_0 \pm \delta\kappa(z)$.

III. FLOQUET TOPOLOGICAL END MODES

The coexistence of the two Floquet end modes necessitates significant global and periodic dimerization conditions. These conditions can be achieved through various settings, such as $\delta\kappa_0 \ll \kappa_0$ and $\delta\kappa_1 \ll \kappa_0$, implying that $\kappa_0 \pm \delta\kappa_0 \pm \delta\kappa(z) \simeq \kappa_0$. Consequently, the coupling length is primarily controlled by κ_0, which can be expressed as $l_c \simeq \pi/2\kappa_0$. Moreover, $\delta\kappa_0$ and $\delta\kappa(z)$ contribute primarily to global and periodic dimerization, respectively. To elucidate their impact on the propagation process, we introduce the effective Hamiltonian H_{eff}. The dynamic process along the periodic bending waveguides can be characterized by the time operator $U(z, z_0) = \hat{T} e^{-i\int_{z_0}^{z} H(z)dz}$, where $\hat{T}$ is the time-order operator,

and z_0 is the initial position. Due to the bending of waveguides, the time ordering operator is periodic, i.e., $U(z_2, z_1) = U(z_2 + \Lambda, z_1 + \Lambda)$. To describe the propagation of the electric field through the model, we assume that $z_0 = 0$ and define $U(z, 0)$ as $U(z)$, which yields $U(z + n\Lambda) = U(z)[U(\Lambda)]^n$ for $z \in [0, \Lambda]$. It implies that after the electric field propagates through the system for one period, the time evolution operator is $U(\Lambda)$. To derive the effective Hamiltonian, we take the natural logarithm of $U(\Lambda)$ and divide it by Λ/i, resulting in $H_{\text{eff}} = (i/\Lambda)\ln U(\Lambda)$ [32,39,53–55]. The formulation enables us to investigate the dynamics of the electric field and the topological properties of the model. Consequently, we can obtain the quasienergy spectrum of one period by determining the eigenvalues ϵ of H_{eff}. Two cases of quasienergy spectra are illustrated in Figs. 1(c) and 1(d). To investigate the conditions that allow the coexistence of the two topological end modes, we vary the coupling strength κ. Considering that the effective coupling strength κ is predominantly determined by κ_0, $\delta\kappa_0$, and $\delta\kappa(z)$, we can set κ_0 to a fixed value and modify the values of $\delta\kappa_0$ and $\delta\kappa(z)$ to observe their impact on the quasienergy ϵ.

When $\delta\kappa_0 \leqslant 0$, the model exhibits a typical trivial state similar to the trivial SSH model, resulting in the absence of a topological zero state. It is depicted in Figs. 1(a) and 1(c), where $g_1 = g_2$ ($g_o = 0$), which can result in which the maximum value of coupling strength $\kappa_1(z)$ and that of $\kappa_1(z)$ are the same. Consequently, in our model, the existence of topological zero mode is prohibited. On the other hand, in the case of $\delta\kappa_0 > 0$, the trivial state undergoes a transition to a nontrivial state. When $g_1 > g_2$ ($g_o > 0$), as shown in Figs. 1(b) and 1(d), the maximum of coupling strength $\kappa_1(z)$ is smaller than that of $\kappa_2(z)$. This leads to the emergence of quasienergy bands corresponding to the topological zero and π end states, allowing for the coexistence of the two topological end modes. Therefore, the configuration supports a nontrivial state and enables the existence of the topological zero mode.

Regarding $\delta\kappa(z)$, its value is affected by $\delta\kappa_1$ and Λ. Unlike the parameter $\delta\kappa_0$, the value of $\delta\kappa_1$ has no significant influence on periodic dimerization. The reason for the difference is that when the periodic staggered coupling strength is negative ($\delta\kappa_1 < 0$), we can transform it into an equivalent pattern with positive coupling ($\delta\kappa_1 > 0$) and a π phase shift. According to the Floquet explanation, $-\delta\kappa_1 \cos(2\pi z/\Lambda + \theta)$ is equivalent to $\delta\kappa_1 \cos(2\pi z/\Lambda + \pi + \theta)$, which means that a pattern with negative dimerization coupling ($\delta\kappa_1 < 0$) and gauge (θ) is equivalent to a pattern with positive dimerization coupling ($\delta\kappa_1 > 0$) and gauge ($\theta + \pi$). In addition, the parameter Λ plays a crucial role in controlling both global and periodic dimerization. The influence of Λ on the global and periodic dimerization can be explained by comparing its magnitude with the coupling length l_c. To do so, we introduce the Floquet Hamiltonian and quasienergy spectrum of the system, which provide further insights into the system's behavior.

The Floquet Hamiltonian is a kind of quasienergy spectrum that emerges due to the periodic bending of the model as the electric wave propagates through it [39,56–58]. The wave obeys the equations $[H(z) - i\partial/\partial z\,]|\psi(z)\rangle = 0$, and the solution of the equation satisfies the composed Hilbert space: $\mathcal{H} \otimes \mathcal{Z}$. Here, $\mathcal{H}$ represents the usual Hilbert space, and $\mathcal{Z}$ is the periodic space (resulting from periodic bending in the system), which is spanned by $e^{in2\pi z/\Lambda}$, with n representing the nth Floquet replica. In our study, we consider only the $0, \pm1, \pm2$ replicas. The quasienergy spectrum, related to the quasimomentum k, is truncated for five Floquet replicas, revealing the states of the topological zero quasienergy band and the π quasienergy band. To ensure the influence of the staggered coupling strength, the initial state of the system requires $\delta\kappa_0 > 0$. The Floquet band schematic, as shown in Fig. 2, demonstrates the profound connection between l_c/Λ and quasienergy ϵ. Thus, the Floquet Hamiltonian provides insights into the role of Λ in global and periodic dimerization, shedding light on the underlying dynamics of the system.

In Fig. 2(a), we observe distinct behaviors of the two topological end modes as the l_c/Λ ratio varies. Besides, we calculate the Floquet topological invariants, which can characterize the quasienergy gap at zero or π in a 1D periodically driven system (see the Supplemental Material [52]). The zero end mode appears only when $l_c/\Lambda > 1/2$, exhibiting a gap invariant of $G_0 = 1$. However, beyond the range, the band gap remains closed, indicating that the topological zero mode can only exist stably when $l_c/\Lambda > 1/2$. On the other hand, the quasi-energy spectrum of the topological π end mode exhibits a closed-open-closed pattern as l_c/Λ varies. It is stable only within the range of $1/3 < l_c/\Lambda < 1$, which corresponds to variations in the value of the gap invariant G_π. The specific mode changes can be explained by the quasi-energy spectrum of the Floquet Hamiltonian shown in Fig. 2(b). For instance, when $l_c/\Lambda = 1/3$, the topological quasienergy band gap of the π mode remains closed due to a band touching between the energy bands with $n = 1$ and $n = -2$. However, as the l_c/Λ ratio increases, the energy bands for the photons start to separate from each other. At $l_c/\Lambda = 5/12$, the energy band gap of the π mode opens up, as depicted in the graph. As the ratio further increases, the zero energy band gap also opens up at $l_c/\Lambda = 1/2$ due to the opening of band gaps for two other energy bands ($n = 1$ and $n = -1$). The system can sustain the two topological end modes when it satisfies the aforementioned conditions. However, as the ratio continues to increase, the quasienergy bands will once again intersect. As shown in the figure, the gap for the π mode closes at $l_c/\Lambda = 1$, indicating that the topological π mode can only exist stably within the range $1/3 < l_c/\Lambda < 1$. In summary, the system can support the topological zero and the π end mode simultaneously only within the range of $1/2 < l_c/\Lambda < 1$.

Through the preceding discussion, we have established the conditions that support the existence of different Floquet end modes. Subsequently, numerical calculations were performed to obtain the projected values by projecting the different Floquet end modes in each instantaneous eigenstate. The projection probabilities at various locations of the waveguide were represented by coloring the instantaneous eigenvalues in the Supplemental Material [52]. Upon observing the results, we can deduce that the topological π mode emerges from an alternating interplay between the boundary modes and bulk modes within one period. Specifically, at the middle part of $n\Lambda$, the state is predominantly influenced by the bulk modes, whereas at $n\Lambda$, the state is primarily determined by the boundary modes. In contrast, the topological zero mode arises from an existing nontrivial topological phase without modulation. From the results, it becomes apparent

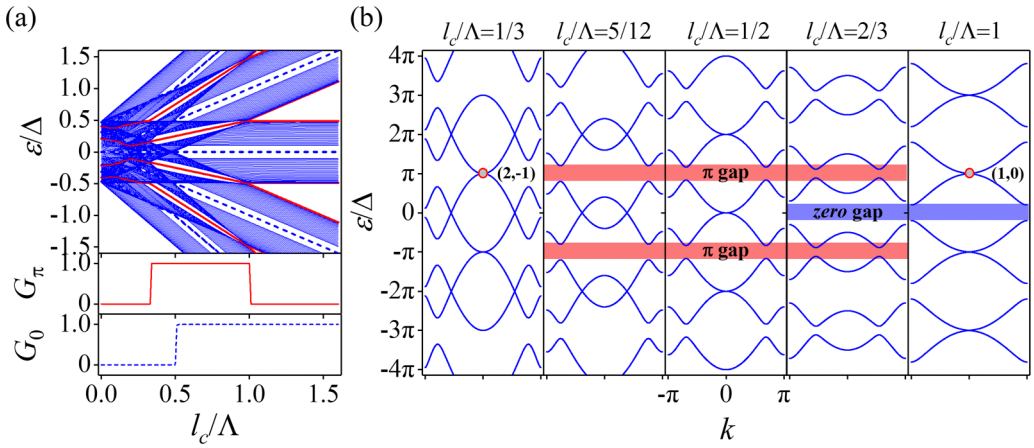

FIG. 2. The figures offer a comprehensive analysis of the influence of different values of l_c/Λ on the quasienergy spectrum, Floquet topological invariants, and the Floquet replicas. Specifically, (a) illustrates the variations in the quasienergy spectrum of the Floquet Hamiltonian and the gap invariants G_π and G_0 of the topological end modes with respect to the change in l_c/Λ. (b) complements this by showcasing the alterations in the Floquet replicas under various modulation frequencies.

that as the electric field propagates along the waveguide, the state is mainly determined by the boundary modes. What's more, when the two kinds of Floquet end modes exist simultaneously throughout the transmission, they interfere with each other, resulting in the electric field at odd Λ being primarily determined by the bulk modes, while at even Λ, it is determined by the boundary modes. This leads to the electric field distribution having twice the period of the model.

IV. FLOQUET INTERFERENCE EFFECT

In the previous discussion, we have determined the appropriate ratio range that supports the coexistence of the two topological end modes. Now, we present the eigenfield distributions of the Floquet zero mode and the π mode in Fig. 3. As depicted in the diagram, the topological zero mode is primarily localized at the curved boundary waveguide, while the topological π mode mainly propagates along the two boundary waveguides. The field distributions of the two topological modes exhibit distinct propagation profiles and overlapping regions. Therefore, when the waveguide model falls within the suitable range, the interference between the two topological boundary modes becomes possible. According to Floquet theory, the topological edge state can be described by the function $\psi_{0(\pi)}(x,z) = u_{0(\pi)}\exp(-i\epsilon_{0(\pi)}z)$, where $u(x,z) = u(x,z+\Lambda)$ represents the micromotion of one period, and ϵ is the corresponding quasienergy of the topological edge state. When the two end modes interfere, the dynamic intensity of the Floquet state can be expressed as

$$\begin{aligned} I_\pm &= [\psi_0(x,z) \pm \psi_\pi(x,z)]^2 \\ &= [\psi_0(x,z)^2] + [\psi_\pi(x,z)^2] \pm 2\Re[\psi_0^*(x,z)\psi_\pi(x,z)] \\ &= [u_0(x,z)^2] + [u_\pi(x,z)^2] \\ &\quad \pm 2\Re[u_0^*(x,z)u_\pi(x,z)]\cos(|\epsilon_0 - \epsilon_\pi|z). \end{aligned} \tag{3}$$

From the formula provided, we can observe that the sum frequency and difference frequency components exhibit the same periodic distribution. Since $|\epsilon_\pi - \epsilon_0| = \pi/\Lambda = \epsilon_\pi$, the final field intensity distribution will repeat with a period of twice the period of the π edge mode, i.e., $I(x,z) = I(x,z+2\Lambda)$, which aligns with the field distribution depicted in Fig. 3. Based on our analysis, we can conclude that the 2Λ-periodic subharmonic arises from the interference of the two topological edge states, which can also be interpreted as a manifestation of the interference process.

V. DYNAMIC CONTROL VIA THE GAP DISTANCES

To verify the discussion on various parameters ($\delta\kappa_0$, $\delta\kappa_1$, Λ), we fabricate the plasmonic waveguide as shown in

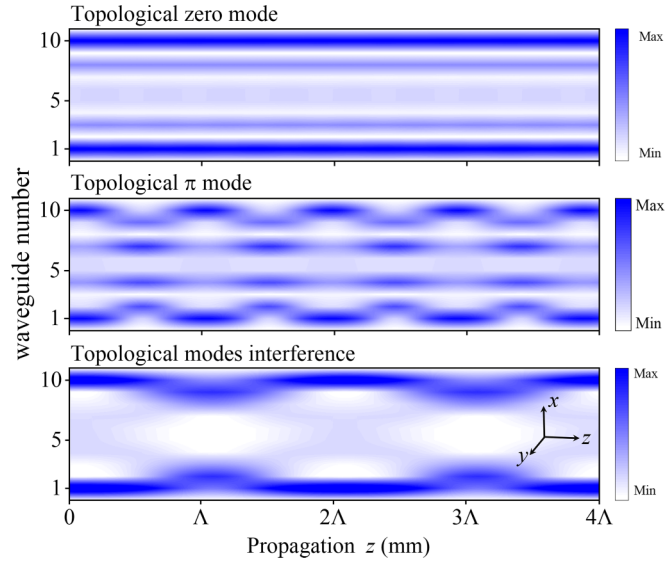

FIG. 3. The figures show the dynamic evolution of the topological end modes in a lattice of ten waveguides. From top to bottom, the distributions are the zero mode, the π mode, and the interference field of the two edge modes. These images illustrate how the topological end modes evolve over time and interact with each other in the waveguide system.

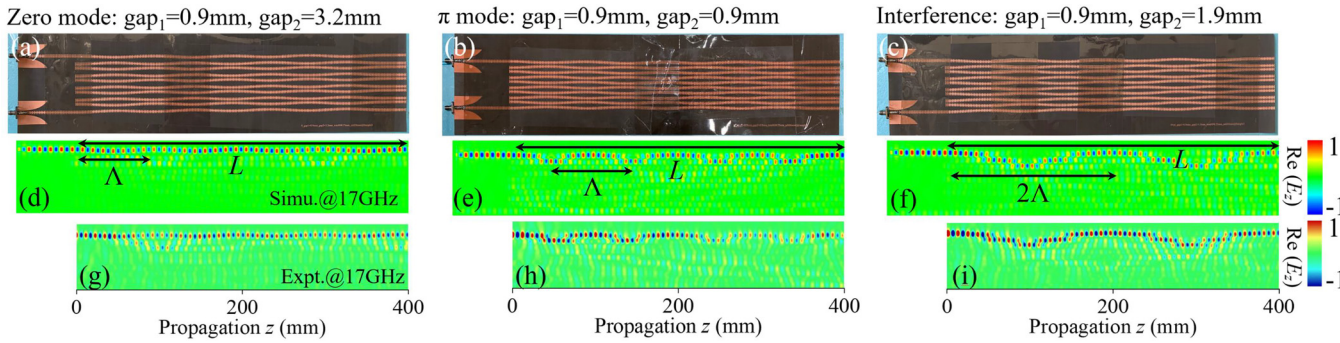

FIG. 4. The figures present the experimental and simulation results for different topological edge states. Schematics (a), (b), and (c) depict the experimental samples with specific parameters that can realize different topological edge states. The simulated electric field E_z distributions for each sample are displayed in schematics (d), (e), and (f) using the CST simulation software. The corresponding experimental results are shown in schematics (g), (h), and (i), and they exhibit good agreement with the simulation results.

Figs. 4(a), 4(b), and 4(c), in which the ultrathin copper strips, with a thickness of 0.018 mm, are printed on a very thin and flexible dielectric film with a thickness of 0.2 mm. The simulation was performed on a model with a length of 400 mm, consisting of four periods (or three periods, as mentioned in the Supplemental Material [52]). The incident electromagnetic frequency was set at 17 GH. For numerical calculations, we utilized the CST simulation software and carefully selected the appropriate parameters to observe the different topological edge modes and their interference effects. Further details of the simulation and experimental setup can be found in the Supplemental Material [52].

We present the simulation field distribution in Fig. 4(d), when the value of g_1 is much larger than g_2 ($g_1 = 3.2$ mm, $g_2 = 0.9$ mm), the ratio l_c/Λ is approximately 1.12, satisfying the condition $l_c/\Lambda > 1$. As a result, the coupling between the neighboring waveguides nearly disappears, making it impossible to support the existence of the π mode. Consequently, the injected microwave only propagates along the boundary waveguide, displaying the characteristics of the topological zero mode while suppressing the topological π mode. On the other hand, in Fig. 4(e), when g_1 is equal to g_2 ($\delta\kappa_0 = 0$) or when the ratio $l_c/\Lambda \approx 0.69$, indicating the absence of a staggering distance, the electric field E_z distribution exhibits the characteristic features of the topological π mode. The injected microwave primarily localizes within the two waveguides at the upper boundary, displaying a periodic oscillation with a period of Λ. Regardless of these two cases, when the model satisfies the condition $1/3 < l_c < 1$ with $\delta\kappa_0 \neq 0$ and has appropriate parameters ($g_1 = 1.9$ mm, $g_2 = 0.9$ mm) with a ratio $l_c/\Lambda \approx 0.92$, the global dimerization and periodic dimerization are sufficient to support the interference between the topological zero and π mode. The subharmonic period-2Λ evolution is depicted in Fig. 4(f). Furthermore, to demonstrate the topological robustness of the interference phenomenon between boundary states, we introduced specific defects to the system and performed rigorous simulation verification (see the Supplemental Material [52]). Moreover, the near-field distributions of E_z components for such a plasmonic waveguide are measured at the frequency of 17 GHz, as illustrated in Figs. 4(g), 4(h), and 4(i), which have excellent agreements.

VI. DYNAMIC CONTROL VIA THE PERIODICAL LENGTHS

To further investigate the impact of the length of one period on the l_c/Λ ratio, we conducted simulations using models with different period lengths. The results are illustrated in Fig. 5, where the gap distance of the model is maintained at $g_1 = 1.9$ mm and $g_2 = 0.9$ mm ($g_1 = 2.5$ mm and $g_2 = 1$ mm in the Supplemental Material [52]); the total number of periods is chosen to be 3, 8, and 16. As depicted in Fig. 5, as the length of one period decreases, the l_c/Λ ratio increases accordingly. The phenomena suggest that by adjusting the number of periods, we can control the ratio l_c/Λ and thereby manipulate the interference effects between the topological edge modes. Understanding the relationship provides valuable insights for the design and engineering of waveguide arrays to achieve specific interference patterns and tailor the properties of topological edge states.

In Fig. 5, the top, middle, and bottom rows represent models with period lengths of 266 mm, 100 mm, and 50 mm, respectively. When the length of one period is 266 mm, the l_c/Λ ratio is approximately 0.346, satisfying the condition $1/3 < l_c/\Lambda < 1/2$. As depicted in the figure, the electric field distribution exhibits the same number of periods as the bending period of the waveguide array, indicating the presence of the topological π mode. As we decrease the length of one period to 100 mm, the l_c/Λ ratio increases to approximately 0.92, meeting the condition $1/2 < l_c/\Lambda \approx 0.92 < 1$.

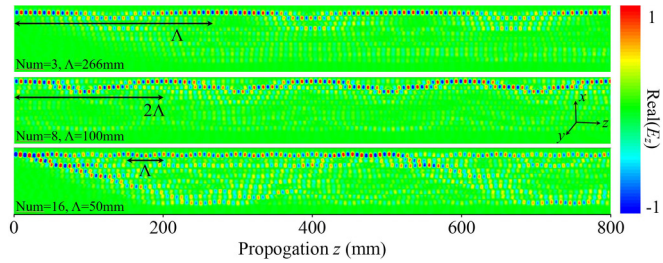

FIG. 5. The figures show the field distributions of the waveguide arrays for various period lengths, with $g_1 = 1.9$ mm and $g_2 = 0.9$ mm. As the period length varies, the field distribution undergoes noticeable changes.

In the scenario, the electric field distribution demonstrates a period that is twice the bending period, signifying the characteristic interference of the two topological modes. Furthermore, as the length of one period is further reduced to 50 mm, the l_c/Λ ratio increases to approximately 1.84, satisfying the condition $l_c/\Lambda > 1$. The field distribution of the waveguide array is predominantly concentrated on the first waveguide. If we continue to increase the l_c/Λ ratio, the model can be described by the static SSH model according to the Floquet theory [32,39]. Hence, we can conclude that as the length of the period decreases, the l_c/Λ ratio increases, and the electric field distributions undergo a similar transformation as when we directly modify l_c.

VII. CONCLUSION

In summary, the study successfully implemented a Floquet-engineering system and observed the emergence of period doubling (2Λ) in a spoof SPPs waveguide. We demonstrated the existence of the exotic 2Λ-periodic subharmonic in staggered periodic curved waveguides, which differs from the nontrivial Floquet π modes in periodic curved waveguides. By applying the Floquet theorem, we analyzed the superposition of electric field distributions of Floquet zero and π modes and confirmed that the interference of these two topological modes in the parent system is the underlying mechanism for the phenomenon.

Moreover, we have identified the required driving period to achieve interval selection of the number of topological modes, which can be verified through the corresponding topological invariant. Furthermore, recent researches have explored the induction of Floquet π modes in other systems, including approaches involving PT symmetry [43] and gauge methods [59]. Overall, our findings contribute to the understanding of Floquet topological physics and open up possibilities for designing and implementing novel waveguide systems with tunable topological properties.

ACKNOWLEDGMENTS

The authors are thankful to Prof. Shining Zhu, Prof. Tao Li, and Prof. Chaohong Lee for helpful discussions. Q. Cheng is supported by the National Natural Science Foundation of China (Grants No. 12174260 and No. 11874266), by the Shanghai Rising-Star Program (Grant No. 21QA1406400) and by the Shanghai Science and Technology Development Fund (Grants No. 21ZR1443500 and No. 21ZR1443600). H.W. is supported by the National Natural Science Foundation of China (Grant No. 12104217). Y.K. is supported by the National Natural Science Foundation of China (Grant No. 12275365) and the Natural Science Foundation of Guangdong (Grant No. 2023A1515012099).

Q.C. conceived the idea. Q.C., C.J., S.Z., A.X., and L.D. prepared the samples and performed the experiment. C.J. conducted numerical simulations. Q.C., C.J., H.W., and Y.K. contributed to the writing of the paper, Q.C., H.W., Y.K., and S.Z. supervised the entire study and all authors took part in the discussion and revision and approved the final copy of the manuscript.

The authors declare no competing interests.

[1] I. L. Garanovich, S. Longhi, A. A. Sukhorukov, and Y. S. Kivshar, Light propagation and localization in modulated photonic lattices and waveguides, Phys. Rep. **518**, 1 (2012).

[2] J. Cayssol, B. Dóra, F. Simon, and R. Moessner, Floquet topological insulators, Phys. Status Solidi RRL **7**, 101 (2013).

[3] L. Lu, J. D. Joannopoulos, and M. Soljačić, Topological photonics, Nat. Photon. **8**, 821 (2014).

[4] T. Ozawa, H. M. Price, A. Amo, N. Goldman, M. Hafezi, L. Lu, M. C. Rechtsman, D. Schuster, J. Simon, O. Zilberberg *et al.*, Topological photonics, Rev. Mod. Phys. **91**, 015006 (2019).

[5] D. Smirnova, D. Leykam, Y. Chong, and Y. Kivshar, Nonlinear topological photonics, Appl. Phys. Rev. **7**, 021306 (2020).

[6] M. Segev and M. A. Bandres, Topological photonics: Where do we go from here? Nanophotonics **10**, 425 (2021).

[7] V. Dal Lago, M. Atala, and L. E. F. Torres, Floquet topological transitions in a driven one-dimensional topological insulator, Phys. Rev. A **92**, 023624 (2015).

[8] C. Jörg, C. Dauer, F. Letscher, M. Fleischhauer, S. Eggert, S. Linden, and G. von Freymann, Limits of topological protection under local periodic driving, Light Sci. Appl. **8**, 63 (2019).

[9] D. Xiao, M.-C. Chang, and Q. Niu, Berry phase effects on electronic properties, Rev. Mod. Phys. **82**, 1959 (2010).

[10] M. Atala, M. Aidelsburger, J. T. Barreiro, D. Abanin, T. Kitagawa, E. Demler, and I. Bloch, Direct measurement of the Zak phase in topological Bloch bands, Nat. Phys. **9**, 795 (2013).

[11] Y. Zhang, Y. V. Kartashov, F. Li, Z. Zhang, Y. Zhang, M. R. Belić, and M. Xiao, Edge states in dynamical superlattices, ACS Photon. **4**, 2250 (2017).

[12] B. Zhu, H. Zhong, Y. Ke, X. Qin, A. A. Sukhorukov, Y. S. Kivshar, and C. Lee, Topological Floquet edge states in periodically curved waveguides, Phys. Rev. A **98**, 013855 (2018).

[13] A. P. Schnyder, S. Ryu, A. Furusaki, and A. W. W. Ludwig, Classification of topological insulators and superconductors in three spatial dimensions, Phys. Rev. B **78**, 195125 (2008).

[14] M. C. Rechtsman, J. M. Zeuner, Y. Plotnik, Y. Lumer, D. Podolsky, F. Dreisow, S. Nolte, M. Segev, and A. Szameit, Photonic Floquet topological insulators, Nature (London) **496**, 196 (2013).

[15] T. Oka and H. Aoki, Photovoltaic Hall effect in graphene, Phys. Rev. B **79**, 081406(R) (2009).

[16] M. Hafezi, E. A. Demler, M. D. Lukin, and J. M. Taylor, Robust optical delay lines with topological protection, Nat. Phys. **7**, 907 (2011).

[17] P. St-Jean, V. Goblot, E. Galopin, A. Lemaître, T. Ozawa, L. Le Gratiet, I. Sagnes, J. Bloch, and A. Amo, Lasing in topological edge states of a one-dimensional lattice, Nat. Photon. **11**, 651 (2017).

[18] L. Jiang, T. Kitagawa, J. Alicea, A. Akhmerov, D. Pekker, G. Refael, J. I. Cirac, E. Demler, M. D. Lukin, and P. Zoller,

Majorana Fermions in Equilibrium and in Driven Cold-Atom Quantum Wires, Phys. Rev. Lett. **106**, 220402 (2011).
[19] M. Lohse, C. Schweizer, O. Zilberberg, M. Aidelsburger, and I. Bloch, A Thouless quantum pump with ultracold bosonic atoms in an optical superlattice, Nat. Phys. **12**, 350 (2016).
[20] S. Nakajima, T. Tomita, S. Taie, T. Ichinose, H. Ozawa, L. Wang, M. Troyer, and Y. Takahashi, Topological Thouless pumping of ultracold fermions, Nat. Phys. **12**, 296 (2016).
[21] D. Y. H. Ho and J. Gong, Quantized Adiabatic Transport In Momentum Space, Phys. Rev. Lett. **109**, 010601 (2012).
[22] Y. Ke, X. Qin, F. Mei, H. Zhong, Y. S. Kivshar, and C. Lee, Topological phase transitions and Thouless pumping of light in photonic waveguide arrays, Laser Photon. Rev. **10**, 995 (2016).
[23] A. Russomanno, B.-e. Friedman, and E. G. Dalla Torre, Spin and topological order in a periodically driven spin chain, Phys. Rev. B **96**, 045422 (2017).
[24] W. Song, H. Li, S. Gao, C. Chen, S. Zhu, and T. Li, Subwavelength self-imaging in cascaded waveguide arrays, Adv. Photon. **2**, 036001 (2020).
[25] M. Pasek and Y. D. Chong, Network models of photonic Floquet topological insulators, Phys. Rev. B **89**, 075113 (2014).
[26] F. Gao, Z. Gao, X. Shi, Z. Yang, X. Lin, H. Xu, J. D. Joannopoulos, M. Soljačić, H. Chen, L. Lu *et al.*, Probing topological protection using a designer surface plasmon structure, Nat. Commun. **7**, 11619 (2016).
[27] Y. E. Kraus, Y. Lahini, Z. Ringel, M. Verbin, and O. Zilberberg, Topological States and Adiabatic Pumping in Quasicrystals, Phys. Rev. Lett. **109**, 106402 (2012).
[28] Y. E. Kraus, Z. Ringel, and O. Zilberberg, Four-Dimensional Quantum Hall Effect in a Two-Dimensional Quasicrystal, Phys. Rev. Lett. **111**, 226401 (2013).
[29] M. Lohse, C. Schweizer, H. M. Price, O. Zilberberg, and I. Bloch, Exploring 4D quantum Hall physics with a 2D topological charge pump, Nature (London) **553**, 55 (2018).
[30] O. Zilberberg, S. Huang, J. Guglielmon, M. Wang, K. P. Chen, Y. E. Kraus, and M. C. Rechtsman, Photonic topological boundary pumping as a probe of 4D quantum Hall physics, Nature (London) **553**, 59 (2018).
[31] S. Hu, Y. Ke, and C. Lee, Topological quantum transport and spatial entanglement distribution via a disordered bulk channel, Phys. Rev. A **101**, 052323 (2020).
[32] M. Bukov, L. D'Alessio, and A. Polkovnikov, Universal high-frequency behavior of periodically driven systems: From dynamical stabilization to Floquet engineering, Adv. Phys. **64**, 139 (2015).
[33] A. Eckardt and E. Anisimovas, High-frequency approximation for periodically driven quantum systems from a Floquet-space perspective, New J. Phys. **17**, 093039 (2015).
[34] S. Weimann, M. Kremer, Y. Plotnik, Y. Lumer, S. Nolte, K. G. Makris, M. Segev, M. C. Rechtsman, and A. Szameit, Topologically protected bound states in photonic parity–time-symmetric crystals, Nat. Mater. **16**, 433 (2017).
[35] R. W. Bomantara and J. Gong, Quantum computation via Floquet topological edge modes, Phys. Rev. B **98**, 165421 (2018).
[36] R. W. Bomantara and J. Gong, Simulation of Non-Abelian Braiding in Majorana Time Crystals, Phys. Rev. Lett. **120**, 230405 (2018).
[37] Y. Pan and B. Wang, Time-crystalline phases and period-doubling oscillations in one-dimensional Floquet topological insulators, Phys. Rev. Res. **2**, 043239 (2020).
[38] B. Wang, J. Quan, J. Han, X. Shen, H. Wu, and Y. Pan, Observation of photonic topological Floquet time crystals, Laser Photon. Rev. **16**, 2100469 (2022).
[39] Q. Cheng, Y. Pan, H. Wang, C. Zhang, D. Yu, A. Gover, H. Zhang, T. Li, L. Zhou, and S. Zhu, Observation of Anomalous π Modes in Photonic Floquet Engineering, Phys. Rev. Lett. **122**, 173901 (2019).
[40] Z. Cheng, R. W. Bomantara, H. Xue, W. Zhu, J. Gong, and B. Zhang, Observation of $\pi/2$ Modes in an Acoustic Floquet System, Phys. Rev. Lett. **129**, 254301 (2022).
[41] Q. Cheng, Y. Pan, Q. Wang, T. Li, and S. Zhu, Topologically protected interface mode in plasmonic waveguide arrays, Laser Photon. Rev. **9**, 392 (2015).
[42] A. Blanco-Redondo, I. Andonegui, M. J. Collins, G. Harari, Y. Lumer, M. C. Rechtsman, B. J. Eggleton, and M. Segev, Topological Optical Waveguiding in Silicon and the Transition between Topological and Trivial Defect States, Phys. Rev. Lett. **116**, 163901 (2016).
[43] S. Wu, W. Song, S. Gao, Y. Chen, S. Zhu, and T. Li, Floquet π mode engineering in non-Hermitian waveguide lattices, Phys. Rev. Res. **3**, 023211 (2021).
[44] Y. Yu, Y. Song, T. Chen, H. Wang, S. Zhuang, and Q. Cheng, Floquet spectrum and optical behaviors in dynamic Su–Schrieffer–Heeger modeled waveguide array, Chin. Opt. Lett. **19**, 042601 (2021).
[45] X. Shen, T. J. Cui, D. Martin-Cano, and F. J. Garcia-Vidal, Conformal surface plasmons propagating on ultrathin and flexible films, Proc. Natl. Acad. Sci. USA **110**, 40 (2013).
[46] H. F. Ma, X. Shen, Q. Cheng, W. X. Jiang, and T. J. Cui, Broadband and high-efficiency conversion from guided waves to spoof surface plasmon polaritons, Laser Photon. Rev. **8**, 146 (2014).
[47] Q. Cheng, T. Chen, D. Yu, Y. Liao, J. Xie, X. Zang, X. Shen, and Y. Pan, Flexibly designed spoof surface plasmon waveguide array for topological zero-mode realization, Opt. Express **26**, 31636 (2018).
[48] T. Chen, Y. Yu, Y. Song, D. Yu, H. Ye, J. Xie, X. Shen, Y. Pan, and Q. Cheng, Distinguishing the topological zero mode and Tamm mode in a microwave waveguide array, Ann. Phys. **531**, 1900347 (2019).
[49] Y. Yu, W. Song, C. Chen, T. Chen, H. Ye, X. Shen, Q. Cheng, and T. Li, Phase transition of non-Hermitian topological edge states in microwave regime, Appl. Phys. Lett. **116**, 211104 (2020).
[50] Q. Cheng, H. Wang, Y. Ke, T. Chen, Y. Yu, Y. S. Kivshar, C. Lee, and Y. Pan, Asymmetric topological pumping in nonparaxial photonics, Nat. Commun. **13**, 249 (2022).
[51] A. Xie, S. Zhou, K. Xi, L. Ding, Y. Pan, Y. Ke, H. Wang, S. Zhuang, and Q. Cheng, Nonparaxiality-triggered Landau-Zener transition in spoof plasmonic waveguides, Phys. Rev. B **106**, 174301 (2022).
[52] See Supplemental Material at http://link.aps.org/supplemental/10.1103/PhysRevB.108.054310 for the relationship between the coupling constant κ and gap distance; the calculation method for Floquet topological invariants; the projection probabilities at various locations of the waveguide; simulation results of the model with three periods; details of simulation and

experimental setup; simulation results of the model with $g_1 = 2.5$ mm and $g_2 = 1$ mm. It also contains Ref. [39].

[53] T. Kitagawa, E. Berg, M. Rudner, and E. Demler, Topological characterization of periodically driven quantum systems, Phys. Rev. B **82**, 235114 (2010).

[54] M. S. Rudner, N. H. Lindner, E. Berg, and M. Levin, Anomalous Edge States and the Bulk-Edge Correspondence for Periodically Driven Two-Dimensional Systems, Phys. Rev. X **3**, 031005 (2013).

[55] M. Rodriguez-Vega, M. Vogl, and G. A. Fiete, Low-frequency and Moiré–Floquet engineering: A review, Ann. Phys. **435**, 168434 (2021).

[56] A. Gómez-León and G. Platero, Floquet-Bloch Theory and Topology in Periodically Driven Lattices, Phys. Rev. Lett. **110**, 200403 (2013).

[57] F. Nathan and M. S. Rudner, Topological singularities and the general classification of Floquet–Bloch systems, New J. Phys. **17**, 125014 (2015).

[58] R. Roy and F. Harper, Periodic table for Floquet topological insulators, Phys. Rev. B **96**, 155118 (2017).

[59] W. Song, Y. Chen, H. Li, S. Gao, S. Wu, C. Chen, S. Zhu, and T. Li, Gauge-induced Floquet topological states in photonic waveguides, Laser Photon. Rev. **15**, 2000584 (2021).